III. RADIO ASTRONOMY*

Academic and Research Staff

Prof. A. H. Barrett	Prof. D. H. Staelin	R. A. Batchelor
Prof. B. F. Burke	J. W. Barrett	D. C. Papa
Prof. R. M. Price		G. D. Papadopoulos

Graduate Students

M. S. Ewing	P. C. Myers	P. R. Schwartz
H. F. Hinteregger	P. W. Rosenkranz	D. L. Thacker
P. L. Kebabian	J. E. Rudzki, Jr.	J. W. Waters
C. A. Knight		A. R. Whitney

A. PRELIMINARY RESULTS FROM THE 1970 AIRBORNE METEOROLOGY EXPEDITION

During the month of June 1970, the engineering prototype of the Nimbus-E microwave spectrometer, a prototype of the Nimbus E-infrared temperature profile radiometer, and a scanning microwave radiometer, together with several auxiliary experiments, were flown in a Convair 990 based at Ames Research Center (NASA), Moffett Field, California. Experimenters from the Research Laboratory of Electronics, M.I.T., the Jet Propulsion Laboratory, the Environmental Science Service Administration, and the Goddard Space Flight Center participated. Ten flights were made over various terrain and cloud conditions, including two flights over Arctic ice and one over the Gulf of Mexico. This report presents some of the results of processing the microwave spectrometer data to obtain an estimate of the temperature profile and other parameters of the atmosphere below the aircraft.

The microwave spectrometer, which was built at the Jet Propulsion Laboratory, has 5 configurationally identical channels with local-oscillator frequencies 22.235, 31.4, 53.65, 54.9, and 58.8 Ghz. These frequencies are in the water-vapor absorption band, a microwave window, and at 3 points in the oxygen absorption band, respectively. The inputs to the Dicke-switched radiometers were switched periodically between the antennas, ambient loads, and temperature-controlled hot loads. The radiometer calibration, that is, the determination of the equivalent temperatures referenced to the antenna of the calibration loads, is the crucial part of the experiment. For this purpose, absorbers at ambient and at liquid-nitrogen temperatures were placed beneath the antennas before and after each flight. A number of difficulties that still have not been resolved were encountered with the nitrogen-cooled absorber, so it was necessary

*This work was supported in part by the National Aeronautics and Space Administration (Grants NGL 22-009-016 and NGL 22-009-421), the National Science Foundation (Grant GP-13056), and California Institute of Technology Contract 952568.

instead to set aside a part of the data, obtained over a known atmosphere, as a calibration for the O_2 channels. The cooled antenna load was used, in spite of the uncertainty, for the calibration of the two low-frequency channels because accurate humidity measurements were not available at the time.

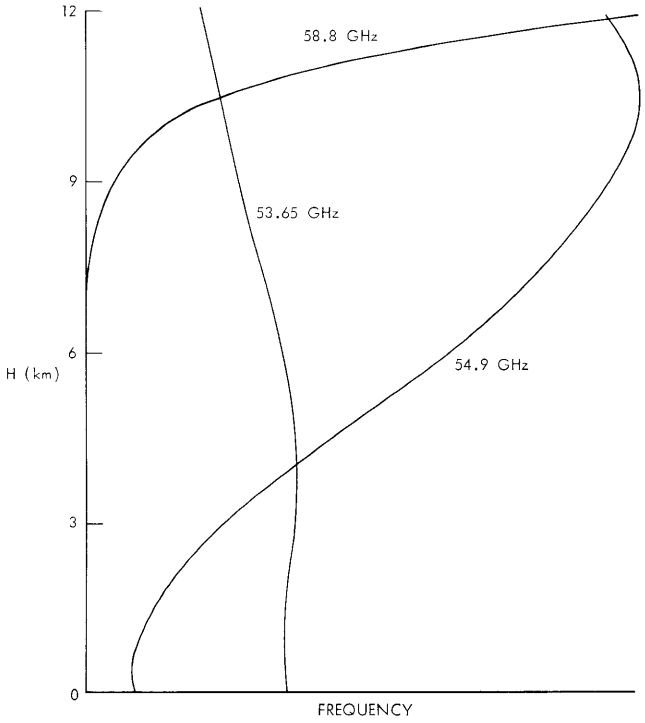

Fig. III-1. Temperature weighting functions.

Figure III-1 shows the temperature weighting functions for the three O_2 channels, from a height of 12 km (approximately 200 mb). These indicate the relative contribution of air temperature as a function of height to the brightness temperature looking down, at each frequency.

The problem can be defined as an inversion of the equation of radiative transfer; the method is a linear regression parameter estimation algorithm. This has been described in detail by Waters and Staelin.[1] Briefly, the estimated vector of parameters $\underline{T}^*$ is given by a linear operation on the data vector $\underline{\Phi}$, which is the vector of microwave antenna temperatures, augmented with a constant for bias:

$$\underline{T}^* = \underline{\underline{A}} \cdot \underline{\Phi}.$$

The matrix of coefficients, $\underline{\underline{A}}$, is determined by minimizing the expected square of the error in the estimate of each parameter, on a statistical basis. Estimates were

made for temperature at intervals of 50 mb, for integrated water vapor, and for integrated liquid water. Figure III-2 and Table III-1 show the rms errors which were computed for these parameters on the basis of the statistics, which were approximately 300 radiosonde records from Oakland, California, Cold Bay, Alaska, and Balboa, Panama. The rms errors for antenna temperatures assumed

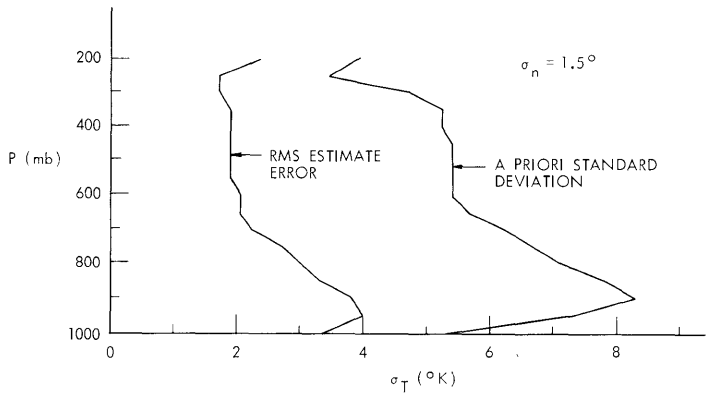

Fig. III-2. Residual estimate errors for temperature.

Table III-1. Residual estimate errors for liquid water and water vapor.

Parameter	RMS Estimate Error (gm/cm^2)	A priori Standard Deviation (gm/cm^2)
Integrated water vapor in clear air	.11	1.15
Integrated water vapor in the presence of clouds	.24	1.71
Integrated liquid water	.01	.06

during these computations were 1.5° for the three O_2 channels and 1° for the other two channels. The surface was assumed to be smooth sea water.

Figures III-3, III-4, and III-5 show atmospheric temperature profiles over water. The profile in Fig. III-3 was in clear air over the Pacific Ocean; in Fig. III-4, in clear air over the Gulf of Mexico; in the case of Fig. III-5, there were heavy clouds associated with a Pacific frontal system between the surface and 500 mb. In each case, the dotted line is the temperature estimate produced from the microwave spectrometer data, and

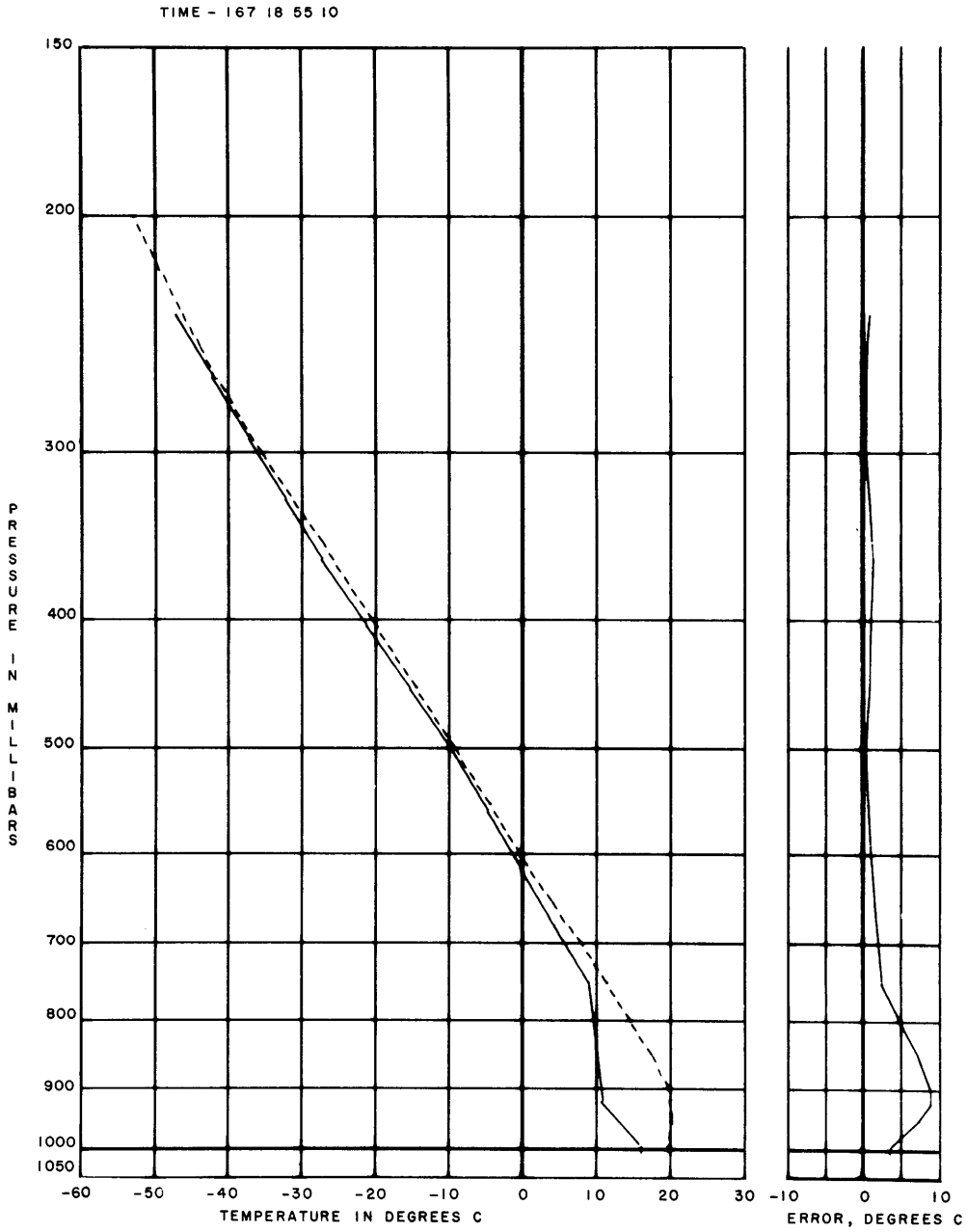

Fig. III-3. Temperature profile over Pacific Ocean.

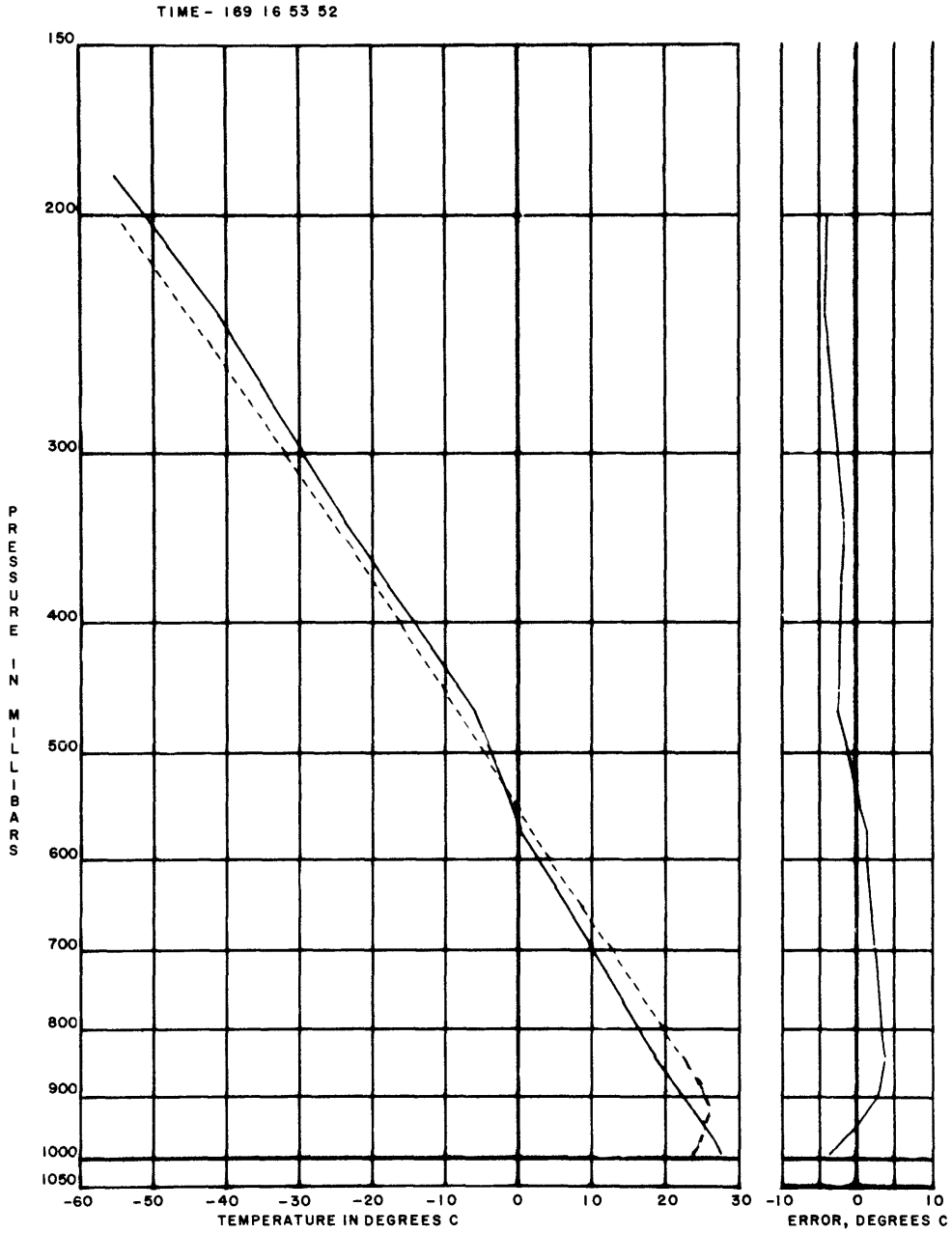

Fig. III-4. Temperature profile over Gulf of Mexico.

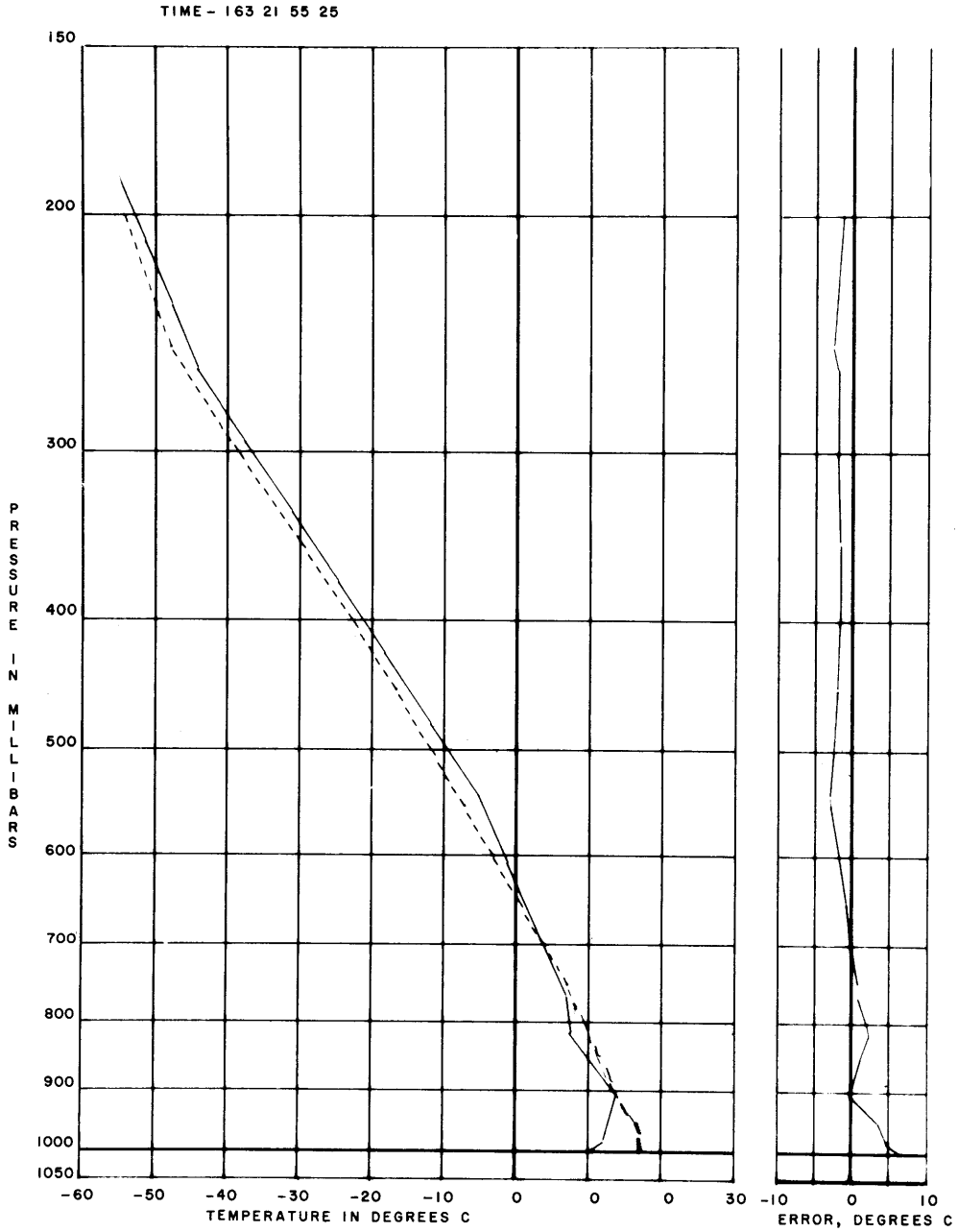

Fig. III-5. Temperature profile over Pacific Ocean.

the solid line is the air temperature measured by the aircraft instrumentation as the plane flew at various altitudes. The difference between the two is plotted on the right. The aircraft temperature sensor has been compared against an infrared measurement of local temperature, which was one of the other experiments on board, and during level flight the two measurements differed by less than 2° C.

As was expected, fine structure in the temperature profile cannot be recovered from the radiometric data. All three graphs show a curving of the estimated temperature profile near the surface, but this is built into the estimate by the choice of statistics. Some large-scale errors are evident in the figures, and these indicate that the calibration is not correct. This is believed to be due to the temperature dependence of the radiometer calibration, and efforts will be made to correct for this.

Estimates for water vapor and liquid water were also made, but accurate direct measurements of these parameters for comparing the estimates have not been established.

P. W. Rosenkranz, D. H. Staelin, F. T. Barath,
J. C. Blinn, E. J. Johnston

[F. T. Barath, J. C. Blinn, and E. J. Johnston are at the Jet Propulsion Laboratory, C.I.T.]

References

1. J. W. Waters and D. H. Staelin, "Statistical Inversion of Radiometric Data," Quarterly Progress Report No. 89, Research Laboratory of Electronics, M.I.T., April 15, 1968, p. 25.

B. WATER-VAPOR EMISSION FROM VARIABLE STARS

Anomalous water-vapor emission at 1.35 cm has been observed from two classes of galactic objects: H II regions and late type stars (Knowles et al.,[1] and Schwartz and Barrett[2]). H II region sources are known to be time variable on time scales of from a few days up to a year (Buhl et al.[3]). At the present time, however, no periodicity, regularity or correlation between water vapor and OH emission has been observed in H II regions (Sullivan[4]). Our observations indicate that, for the class of water-vapor sources associated with late type stars, most are identifiable with long-period optical variables and the variable water-vapor emission from these objects is strongly correlated with the optical and infrared variation of the star.

In addition to the three long-period variables with water-vapor emission that we have discussed elsewhere, W Hya, U Her and R Agl, we have detected three new sources associated with this type of object (Schwartz and Barrett[2]). The Mira variables U Ori and S CrB and the late type short-period variable RX Boo all show microwave water-vapor emission. U Ori is known also to be a main-line OH emission source but does not emit at the 1612-MHz satellite line. The two other sources are apparently not OH sources (Wilson[5]). U Ori and S CrB both obey the rule proposed in our earlier

paper that the microwave line lies between the star's emission and absorption lines in radial velocity. In RX Boo, the microwave line is at approximately the same velocity as the star's absorption lines.

Spectra of U Ori, S CrB and RX Boo are shown in Fig. III-6. It is interesting to note that these three sources are the weakest water-vapor emission sources yet detected. The intrinsic luminosity of RX Boo is at least 10^{-7} that of the strongest water-vapor source, W49.

Observations of variable star/H_2O sources over a period of one year have shown dramatic time variations in the emission line which appear to be correlated with the optical variability of the star. A decrease of almost a factor of ten in the peak flux of R Aql was observed between maximum and minimum optical light; U Her and W Hya have also exhibited similar variations, although of smaller amplitude. Although the data are not complete, it appears as if the other sources also undergo this type of variation. In Fig. III-7a the microwave light curves of R Aql, U Her, and W Hya are shown as a function of optical phase (zero phase is defined as the maximum of the light curve). For comparison, the optical light curves of R Aql and U Her are shown in Fig. III-7b. No light curve is available for W Hya.

The general behavior of long-period variables as a function of phase is quite complicated. The optical and infrared components of the continua of these stars usually vary out of phase, with the infrared lagging the optical by up to 0.2 of a period. Two micron water-vapor absorption bands are usually observed in this type of star and these bands usually vary in intensity with phase. The absorption bands tend to be out of phase, however, with the optical light, with maximum absorption usually occurring at a phase of from 0.4 to 0.6 (Frogel[6]). Our observations indicate that the microwave line only slightly lags the optical maxima, perhaps by as much as 0.1 of a period at the most, and is thus out of phase with the infrared water-vapor absorption bands.

An interesting simplistic model for the behavior of that anomalous water-vapor emission line can be derived by assuming that the inverted length of the masering region $\alpha L = \Lambda$ varies with phase as

$$\Lambda = \frac{\Lambda_o}{2}\left[1 + \cos\left(\frac{2\pi t}{T} + \phi\right)\right],$$

where T is star's period. For a saturated maser, an inhomogeneously broadened line depends in intensity upon the square of the inverted length:

$$I \sim \Lambda^2.$$

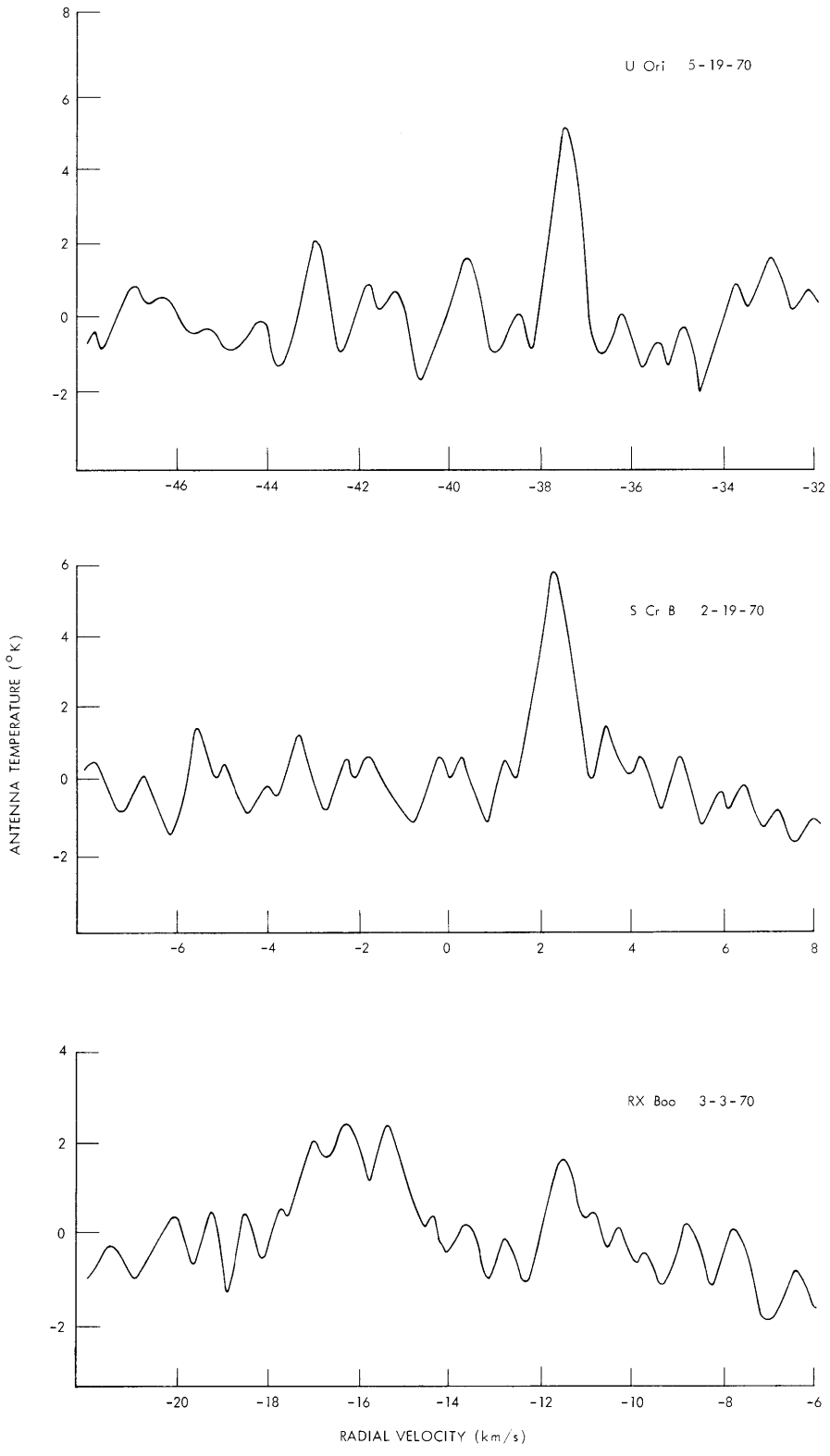

Fig. III-6. Water-vapor spectra of U Ori, S CrB, and RX Boo taken with 0.4 km/s resolution. Haystack Observatory, Lincoln Laboratory, M.I.T., 120' antenna.

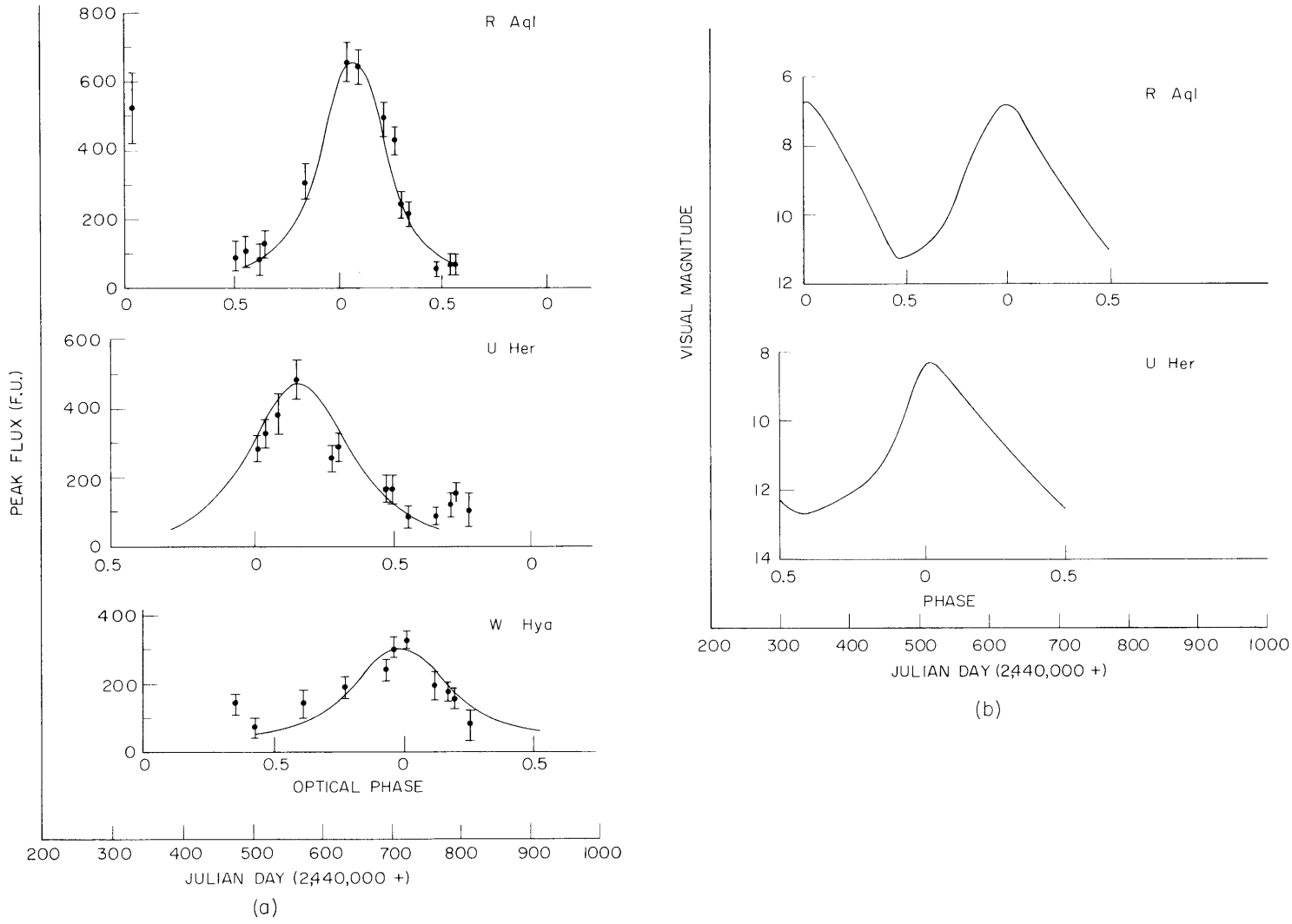

Fig. III-7. (a) Peak flux of the microwave water-vapor line as a function of time for R Aql, U Her, and W Hya. The solid curve represents the model discussed here. (b) Optical light curves of R Aql and U Her provided by the American Association of Variable Star Observers, Cambridge, Mass. (Mayall[7]).

Thus the intensity of the masered emission from a star might be expected to vary as

$$I = \frac{I_o}{4}\left[1+\cos\left(\frac{2\pi t}{T}+\phi\right)\right]^2 + I_1.$$

This curve with I_o, I_1 and ϕ adjusted to maximize the fit is the solid line plotted in Fig. III-7a.

P. R. Schwartz, A. H. Barrett

References

1. S. H. Knowles, C. H. Mayer, A. T. Chueng, D. M. Rank, and C. H. Townes, Science 163, 1055 (1969).
2. P. R. Schwartz and A. H. Barrett, Astrophys. J. 159, L123 (1970).
3. D. Buhl, L. E. Snyder, P. R. Schwartz, and A. H. Barrett, Astrophys. J. 158, L97 (1969).
4. W. T. Sullivan III, a paper presented at the 132nd Meeting of the American Astronomical Society, Boulder, Colorado, 1970.
5. W. J. Wilson, Ph. D. Thesis, Department of Electrical Engineering, M. I. T., May 1970.
6. J. Frogel (to appear in Astrophys. J., 1970).
7. Margaret W. Mayall, Private communication (AAVSO, Cambridge, Mass., 1970).

C. MEASUREMENT OF THERMAL EMISSION FROM MESOSPHERIC O_2

The oxygen molecule contains two unpaired electrons whose resulting magnetic moment interacts with the magnetic moment arising from end-over-end rotation of the molecule and produces a band of resonance lines centered at a frequency of approximately 60 GHz (5 mm wavelength).[1] At the center of this band the terrestrial atmosphere is quite opaque with a transmissivity of less than 10^{-20}, and the full width of the band between 1 Np opacity points is approximately 15 GHz.[2] Below 50 km altitude, individual linewidths are dominated by collisional broadening with halfwidth varying between ~1 MHz at 50 km and ~10^3 MHz at the surface. Above 50 km altitude Zeeman splitting of the individual lines by the Earth's magnetic field produces a halfwidth of ~1 MHz, and the O_2 emission from this region is polarized and anisotropic.[3] On the edge of the O_2 absorption band thermal radiation from the relatively narrow lines in the upper atmosphere can penetrate the lower atmosphere, thereby providing a means of ground-based monitoring of upper atmospheric conditions. The intensity of the radiation received will depend both upon atmospheric temperature and number of

O_2 molecules in the line of sight of the observation. Computations of atmospheric emission for lines on the low-frequency edge of the O_2 absorption band and for conditions as specified by the 1962 U.S. Standard Atmosphere[4] are shown in Fig. III-8. The O_2 absorption coefficient of Meeks and Lilley[2] was used in the calculations. The frequency resolution of Fig. III-8 is too coarse to show fine structure associated with

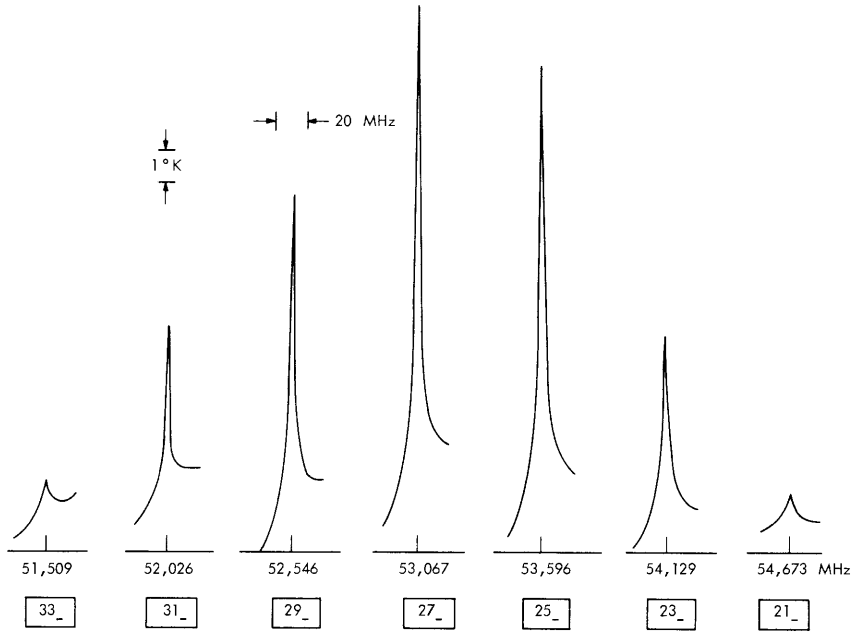

Fig. III-8. Atmospheric emission at high angular momentum O_2 transitions. Calculated for ground-based observation at 0° zenith angle. (80-km upper limit on integrations.)

Zeeman splitting, and the various lines have been shifted in absolute intensity to a common baseline. The vertical scale of the figure is the brightness temperature of the radiation (proportional to intensity in the millimeter wavelength range for atmospheric conditions), and the boxed integers along the horizontal scale are the rotational quantum numbers associated with the various lines. The minus subscript on each quantum number indicates that during a transition the total angular momentum of the molecules changes from $J = N$ to $J = N - 1$, where N is the rotational quantum number. The symmetry of the O_2 molecule allows only odd values of N, and another series of lines, N^+, exist for the transitions $J = N + 1$ to $J = N$.

The 27_- line attributable to upper atmospheric oxygen was reported as observed in absorption against the sun by Kahan.[5] Measurements described here show this line in thermal emission with a signal-to-noise ratio significantly higher than that of Kahan's

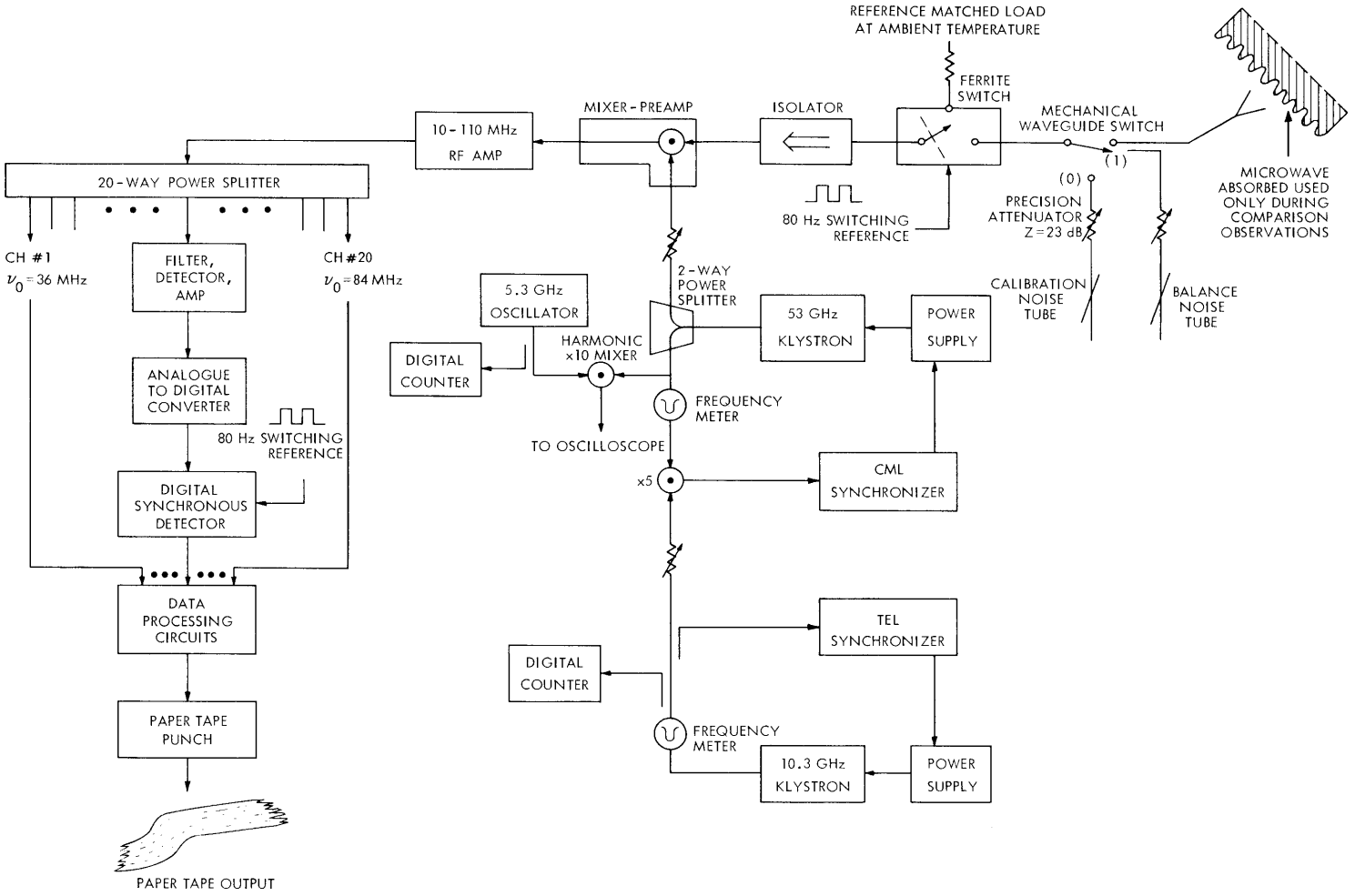

Fig. III-9. Radiometer spectrometer for measurements reported here.

data. A block diagram of the radiometer-spectrometer used for the measurements is shown in Fig. III-9. A conventional Dicke-switched superheterodyne microwave radiometer was used with a 10° beam-width standard gain horn as an antenna. The radiometer had a double-sideband noise temperature of 10,000°K and no intermediate frequency image rejection. The local oscillator was frequency-stabilized by a two-stage feedback loop whose frequency standard was the internal reference for the first-stage synchronizer. Measured frequency stability was better than our measurement accuracy of 0.1 MHz at 53,000 MHz and completely adequate for the experiment as the resolution of the spectrometer was 1.0 MHz. Spectral resolution of the radiation was performed by a bank of twenty filters in the intermediate-frequency section of the radiometer covering the frequency range 35 to 85 MHz. The outer ten filters had full-widths at half-power of 4 MHz and the inner ten had full-width of 1 MHz. Each filter was a single-pole RLC circuit and overlapped its neighbor at the half-power point. The detected output of each of the filters was connected to one channel of a digital synchronous-detector system.[6] This system recorded data on punched paper tape which could then be analyzed by computer.

Measured atmospheric spectra at the 27_- O_2 transition frequency for observations at 10° and 60° elevation angles are shown in Fig. III-10. (The calculated spectral line intensity of Fig. III-10 is half the brightness temperature of the radiation as the radiometer calibration signal appeared in both the image and signal RF passbands, whereas the spectral line radiation appeared only in the signal passband.) Also shown are calculated spectra for these elevations. Detailed agreement between the experimental and calculated spectra is not expected because (i) in the calculation Zeeman splitting was neglected; this will change the shape of the line to a flat-topped feature with width as indicated in Fig. III-10, and (ii) the upper limit on integrations for these calculations was selected somewhat arbitrarily at 80 km. For sea-level observations the strongest signal from the mesospheric 27_- transition occurs at an elevation angle of 90°, the elevation at which lower atmospheric absorption has its minimum value of 1.3 Np. At 10° elevation the mesospheric radiation is reduced in amplitude by more than two orders of magnitude from its 60° elevation value, and can barely be distinguished on the scale of Fig. III-10. The observations described here were made during clear sky conditions between 7 July and 15 July 1970 from the roof of the Compton Laboratory building at the Massachusetts Institute of Technology. The spectrum of Fig. III-10a has an equivalent integration time of approximately 2 hours, and that of Fig. III-10b an integration time of approximately 1 hour. Because of time spent for calibration and comparison measurements, the actual observing time was five times the equivalent integration time. The ripples in the 10° elevation spectrum, Fig. III-10b, are compatible with the theoretical radiometer noise and indicate the accuracy of the measurement. It should be noted that the frequency of the spectral line observed here

is in good agreement with the recently calculated value of 53,066.8 MHz by Wilheit,[7] and differs by less than 3 MHz from the values given by Kahan[5] and by Meeks and Lilley.[2]

The method of obtaining a spectrum consisted in repeating cycles, each of which had ten 4-min steps. At the end of each step the contents of the digital synchronous detectors were recorded on punched tape. The first two steps of a cycle were spent for calibration with the mechanical waveguide switch of Fig. III-9 in position (0), and the calibration noise tube first off and then on. The 20,000°K noise tube attenuated by a factor of 200 gave a 100°K calibration signal, which is the intensity reference for all experimental spectra described here. (The components in the calibration circuit had values specified to an accuracy better than ±10%, which is within the accuracy of the measurements.) The next eight steps in the observing cycle were spent with the mechanical switch in position (1) connecting the radiometer to the horn antenna. On alternate steps the horn was covered with a block of waveguide absorber for a comparison spectrum. On steps when the horn was uncovered, balance noise was added so that millimeter wave radiation entering the mechanical switch had intensity approximately equal that from the reference matched load on the ferrite switch. In this manner, sensitivity to radiometer gain fluctuations is reduced, since the synchronous detectors measure only differences with respect to the reference load. Computer analysis of the data then calibrated the spectra in terms of the 100°K calibration signal and subtracted the comparison spectra (obtained with the absorber in front of the horn) from the signal spectra (obtained with the horn unblocked). Data from many cycles were then averaged to reduce noise. During each observing session, short observations were made without balance noise to measure the absolute intensity of the atmospheric radiation. The absolute intensity measurements indicated in Fig. III-10 are accurate to ±10°K.

Several tests were performed to make sure the observed spectral feature was not due to instrumental effects. (The narrowness of this feature is in itself a significant test as it has a Q of ~10,000 – much higher than expected from any components in the millimeter wave circuitry.) The local-oscillator frequency was shifted and the position of the line in the spectrometer channels was observed to change as expected for a feature at 53,066.8 MHz; this insured that the line was not due to any instrumental feature anywhere in the system behind the mixer, and also proved that the line was at that frequency and not the image frequency of 52,946.8 MHz. The local oscillator was also changed so that no line position was in the IF passband and no line was observed. Observations were then made with the balance noise adjusted so that millimeter wave radiation entering the mechanical switch was in one case hot, and in the other case cold with respect to ambient. Any instrumental feature behind the coupler for the balance noise should reverse polarity for these two cases. The observed feature was the same polarity and amplitude in both cases, thereby proving that it came from in front of the balance coupler. Finally, the waveguide section connecting the horn to the balance

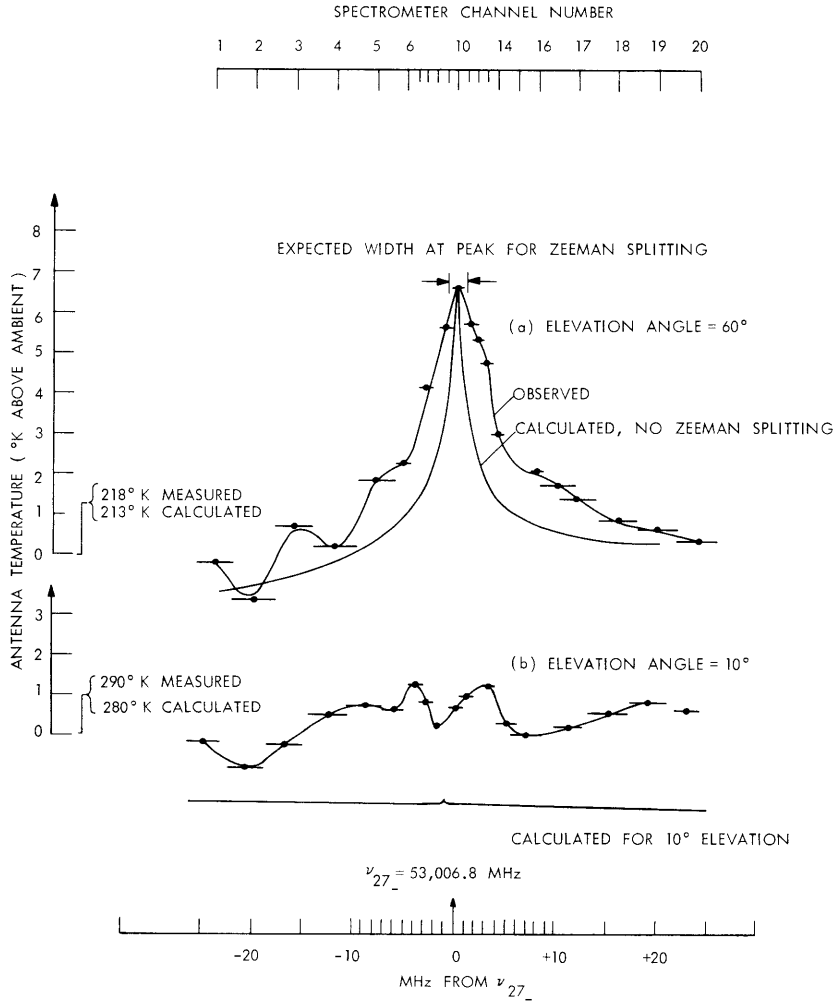

Fig. III-10. Measured atmospheric emission spectrum near 53,007 MHz at two elevation angles.

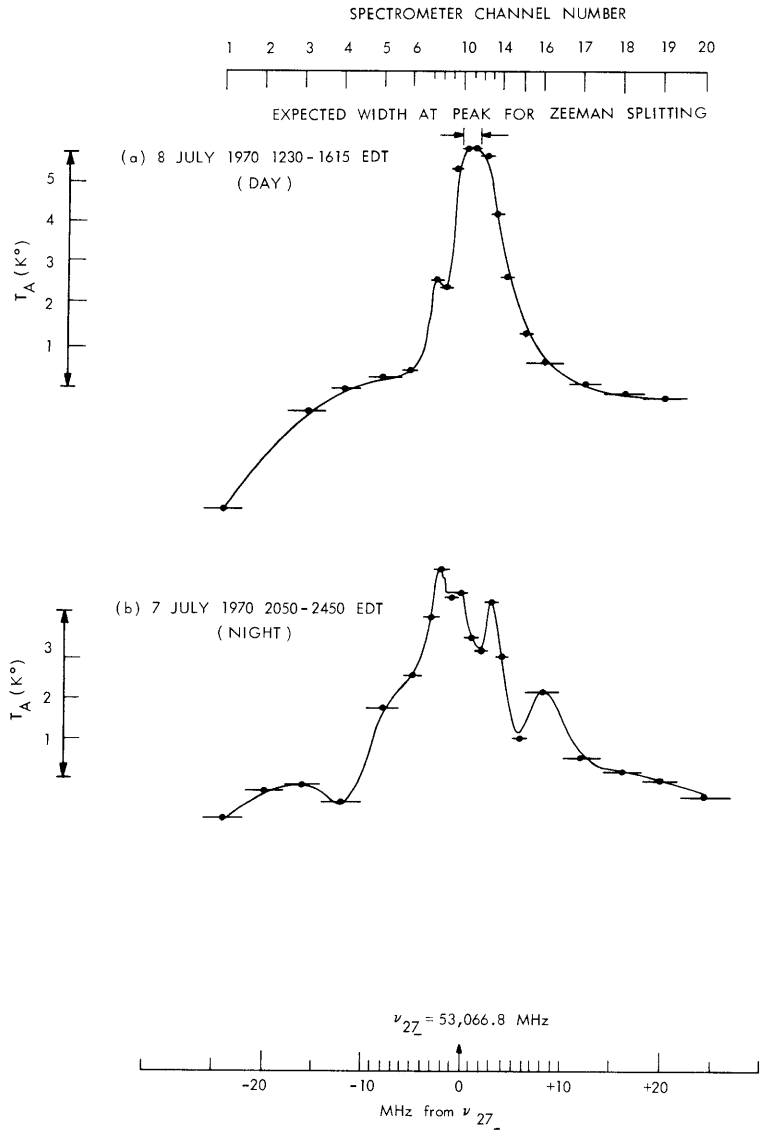

Fig. III-11. Measured diurnal change in atmospheric emission at the ν_{27_-} oxygen line.

coupler was changed from a 60° bend to a 10° bend and a reflector plate was positioned in front of the horn to give an effective observation angle of 60°. The spectrum obtained in this manner was identical, within measurement accuracy, to that obtained with the horn at 60° elevation. These tests, plus the correct elevation dependence shown in Fig. III-10, prove that the spectral feature is not instrumental.

The 60° elevation spectrum of Fig. III-10 is an average of approximately equal daytime and nighttime observations. Fig. III-11 shows separate spectra obtained during night and day. The daytime spectrum is significantly narrower and slightly stronger than the nighttime spectrum, thereby indicating a warmer upper atmosphere during the day. The width of the daytime feature indicates that it originated from altitudes above approximately 50 km. Because of demands by other projects, sufficient time with the electronic equipment was not available to check whether the diurnal variation shown in Fig. III-11 is repeatable. This variation is, however, in phase with radar measurements of atmospheric temperature at 250 km which show a 30% diurnal variation with warmest temperatures at 1600 local time.[8] Individual spectra obtained during our observations suggest significant variations in upper atmospheric temperature over a time period of 1 hour, but the sensitivity of the radiometer used for these observations was not adequate to make a definite statement concerning these variations. With state-of-the-art components – the radiometer used here was constructed from components available in our laboratory at the time – it should be possible to construct a radiometer more sensitive by a factor of ten. Such an instrument should provide convenient ground-based measurements of atmospheric temperature for altitudes between the regions now measured by balloon and by radar.

To quantitatively predict the ultimate accuracy in inferring mesospheric temperature by the technique described here, the matrix theory of radiative transfer developed by Lenoir,[3] or a similar theory, must be used and Zeeman-splitting of the O_2 transitions taken into account. The high-rotational angular-momentum states that produce the transitions are quite sensitive to temperature through molecular energy-level population by collision: a 1% change in atmospheric temperature produces a 5% change in intensity for the 27_- line. Other O_2 transitions, those shown in Fig. III-8 and the corresponding lines on the high-frequency side of the O_2 band, have a slightly different temperature dependence, and many of these lines are sufficiently intense to measure radiometrically from the ground. Altitude resolution, however, is expected to be poor above 50 km because the individual Zeeman components (159 components for the 27_- transition) are smeared by Doppler broadening and the over-all linewidth is only very slightly dependent on altitude. Calculations that include the Zeeman effect are now being performed to numerically test the feasibility of this method for determining upper atmospheric temperature.

I am indebted to M. L. Meeks for suggesting the possibility of measuring the

$27_- O_2$ transition, to J. W. Barrett for engineering the frequency stabilization of the local oscillator in the radiometer, and to D. H. Staelin and A. H. Barrett for helpful discussions.

J. W. Waters

References

1. J. H. Van Vleck, "The Absorption of Microwaves by Oxygen," Phys. Rev. 71, 413 (April 1, 1947).
2. M. L. Meeks and A. E. Lilley, "The Microwave Spectrum of Oxygen in the Earth's Atmosphere," J. Geophys. Res. 68 (6), 1683 (March 15, 1963).
3. W. B. Lenoir, "Microwave Spectrum of Molecular Oxygen in the Mesosphere," J. Geophys. Res. 73 (1), 361 (January 1, 1968).
4. Handbook of Geophysics and Space Environments (McGraw-Hill Book Company, New York, 1965).
5. W. Kahan, "Detection of the Microwave ν_{27-} Line of Molecular Oxygen Produced in the High Atmosphere," Nature 195, 30 (July 7, 1962).
6. L. P. A. Henckels, "A Digital Output Unit for a Multichannel Radiometer," S. M. Thesis, Department of Electrical Engineering, M. I. T., May 1968.
7. T. T. Wilheit, Jr., "Studies in Microwave Emission and Absorption by Atmospheric Oxygen," Ph. D. Thesis, Department of Physics, M. I. T., February 1970.
8. J. S. Nisbet, "Neutral Atmospheric Temperatures from Incoherent Scatter Observations," J. Atmos. Sci. 24, 586 (September 1967).

D. SEARCH FOR INTERSTELLAR SULFUR MONOXIDE

On August 4, 5, 6, 14, 15 and 16, 1970, observations of several galactic radio sources were made with the 37-m Haystack antenna to search for the J = 0, K = 1 to J = 1, K = 0, 30.00016 GHz[1] ground-state transition of the SO radical. No line was detected.

The total-power radiometer was constructed and installed in two weeks. It comprised a crystal-mixer front end, a phase-locked klystron, and an IF whose output was fed into the new Haystack digital correlator. The analog-to-digital conversion of the detector output voltage before correlation eliminated the need for Dicke switching. The observing bandwidth was determined by the correlator to be either 4 MHz or 20 MHz. Typical system temperature was 2000°K, single-sideband.

The 20-MHz bandwidth was used to observe SO and the H recombination line at 29.7 GHz. Interference, which may be due to local television station carrier signals, made interpretation of the spectra difficult, however.

The results of the observations with the 4-MHz bandwidth are presented in Table III-2. We used the following observing procedure: Calibration with a gas tube attenuated to 100°K at the start of each new source (approximately every 4 hours); then alternation between 10-min on-source runs and 10-min off-source runs. An

Table III-2. Results of observations of galactic radio sources.

Date (1970)	Source	Duration (h)	Velocity Range km/s	T_{sys} (°K)	ΔT_{pp} (°K)
8/4	W3	2.0	-65 → -25	1900	0.8
8/4	Ori A	1.2	-20 → 20	2070	1.4
8/5	Sgr B2	0.8	40 → 80	2080	1.6
8/5	Cas A	1.3	-20 → 20	1770	1.2
8/6	W75 (N)	1.3	20 → 60	1840	0.9
8/6	Sgr B2	1.3	40 → 80	2060	1.1
8/6	Sgr A	0.8	40 → 80	2060	1.4
8/15	W75 (N)	3.8	20 → 60	2640	0.9
8/16	Ori A	4.0	20 → 60	1800	0.9

azimuth offset of +1.0° was used for the off-source runs. The differences between the on-source and off-source spectra were averaged together for all runs free of serious interference. The listed duration is the total time length of on-source runs included in the average. The range of Doppler-shifted frequencies chosen to fall within the 4-MHz band corresponds to the range of SO velocities (with respect to the local standard of rest) listed in Table III-2. For each source, the observed velocity range includes velocities at which OH or H_2O radio emission has been detected. The peak-to-peak temperature, ΔT_{pp}, was measured near the band center of the mean-difference spectrum. The system temperature, T_{sys}, single-sideband, was measured at the time of calibration.

We wish to thank the staff of the Haystack Observatory, of Lincoln Laboratory, M.I.T., for engineering and observing assistance.

A. H. Barrett, J. W. Barrett, P. C. Myers,
D. C. Papa, P. R. Schwartz

References

1. F. X. Powell and D. R. Lide, J. Chem. Phys. 41, 1413 (1964).

E. OBSERVATIONS OF PULSAR SPECTRA

1. Introduction

Observations of pulsar spectra yield information about the intrinsic radiation properties of pulsars, and about the intervening interstellar medium. In an effort to separate and study these two aspects of pulsar spectra, we have observed since 1968 the

spectra of those pulsars within the range of the National Radio Astronomy Observatory's 300 ft transit telescope in Green Bank, West Virginia. The spectrometers each had 50 channels with bandwidths of 100, 30, or 10 kHz, or had 40 channels with bandwidths of 1 MHz. The center frequencies of the filter banks ranged from 110 MHz to 550 MHz, and all 40 or 50 channels were sampled with 8-bit accuracy every 30 ms. Subsequent computer analysis yielded the spectra of individual and average pulses. Additionally, in May 1970, both the 300 ft transit telescope and the 140 ft fully steerable telescope in Green Bank were used in conjunction with the 384-channel autocorrelation receiver to achieve frequency resolution as high as 1 kHz.

The present report describes the results of manual analyses of the spectra of four pulsars, CP0328, CP0834, CP1133, and CP1919. A more complete analysis of all of the spectral data is in preparation.

2. Widths of Spectral Features

Typical data obtained with the multichannel filter systems are presented in Fig. III-12. These data were processed by computer, displayed on a cathode-ray tube, and then photographed. Each resolution element in these photographs represents the average of several pulses within a single channel. The three light levels represent relative pulse energy thresholds of 1, 2, and 4. Figure III-12 illustrates how the spectral features in each pulsar develop and change.

Similar data derived from the autocorrelation technique are given in Fig. III-13. The two light levels represent intensity levels in the ratio of 2 to 1. The photographs show only 364 of the 384 frequency channels, the rest have been blanked out because of their greater noise.

One parameter of interest in these spectra is the frequency dependence of spectral feature width. Feature widths were determined by averaging the visually determined instantaneous full widths at half-maximum, B, for a large number of spectral features at each frequency. Typical feature widths observed with the autocorrelator for these four pulsars are listed in Table III-3 as a function of frequency and are plotted in Fig. III-14. The feature widths B are assumed to vary as ν^{α}. Least-squares fits for α yield the numbers in Table III-3. The quoted errors are estimated maximum deviations from the mean fit. The three pulsars, excluding CP1133, are fairly consistent with the value $\alpha = 4$. A ν^4 dependence is generally consistent with the results reported by Rickett,[1] Staelin,[2] and Lang,[3] and apparently inconsistent with those reported by Huguenin et. al.[4] Some of the widths reported here are less than those reported by others, possibly because a cluster of narrow features can resemble a single broad feature.

A ν^4 dependence of feature width is predicted by scintillation theory. In particular, the ν^4 dependence follows if we assume that the antenna intercepts rays that

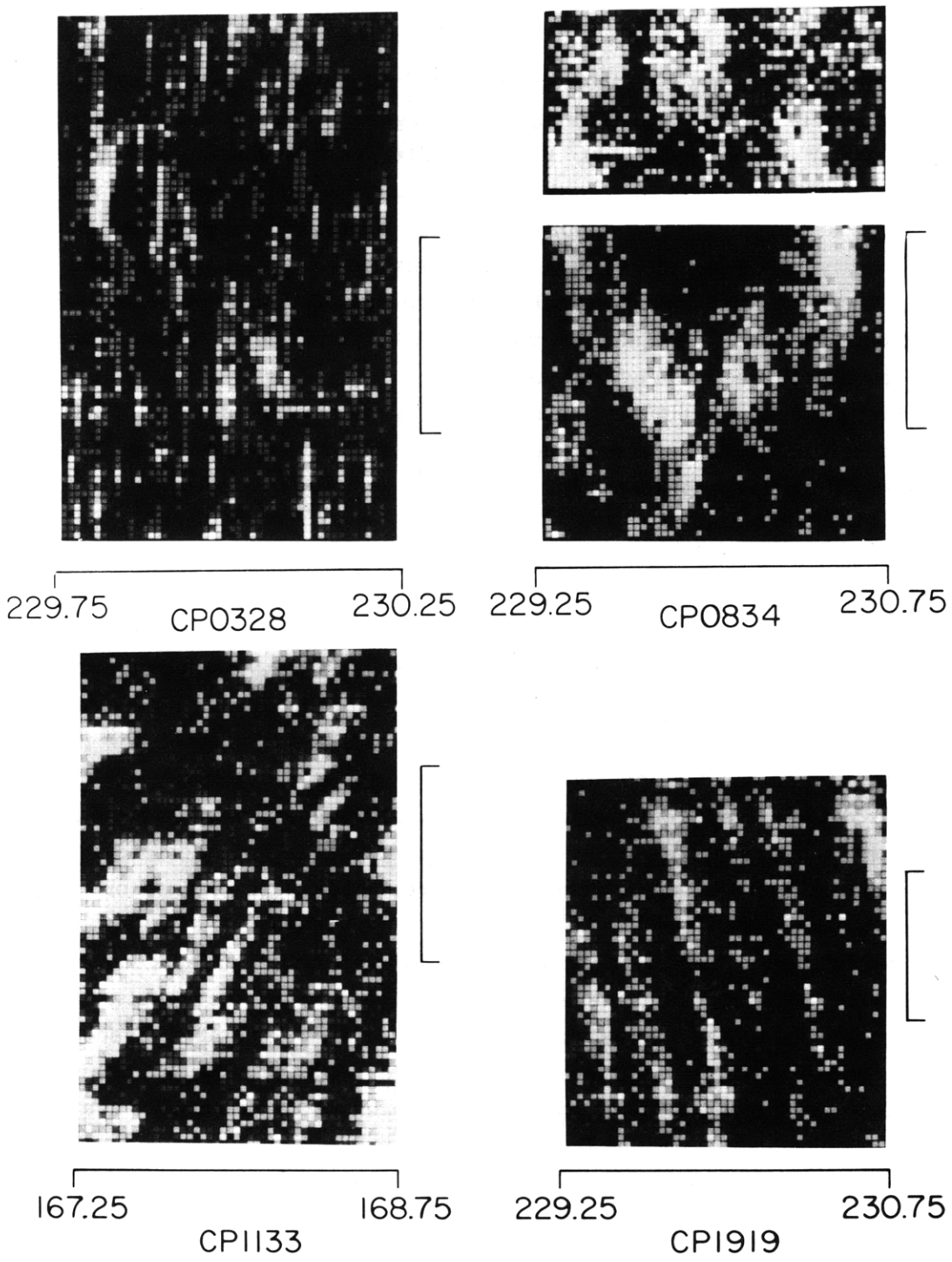

Fig. III-12. Representative dynamic spectra for CP0328, CP0834, and CP1919 as observed with 50-channel spectrometers. The light levels represent relative power thresholds of 1, 2, and 4, in order of increasing brightness. Time increases from top to bottom, and the scale markers represent 10 min.

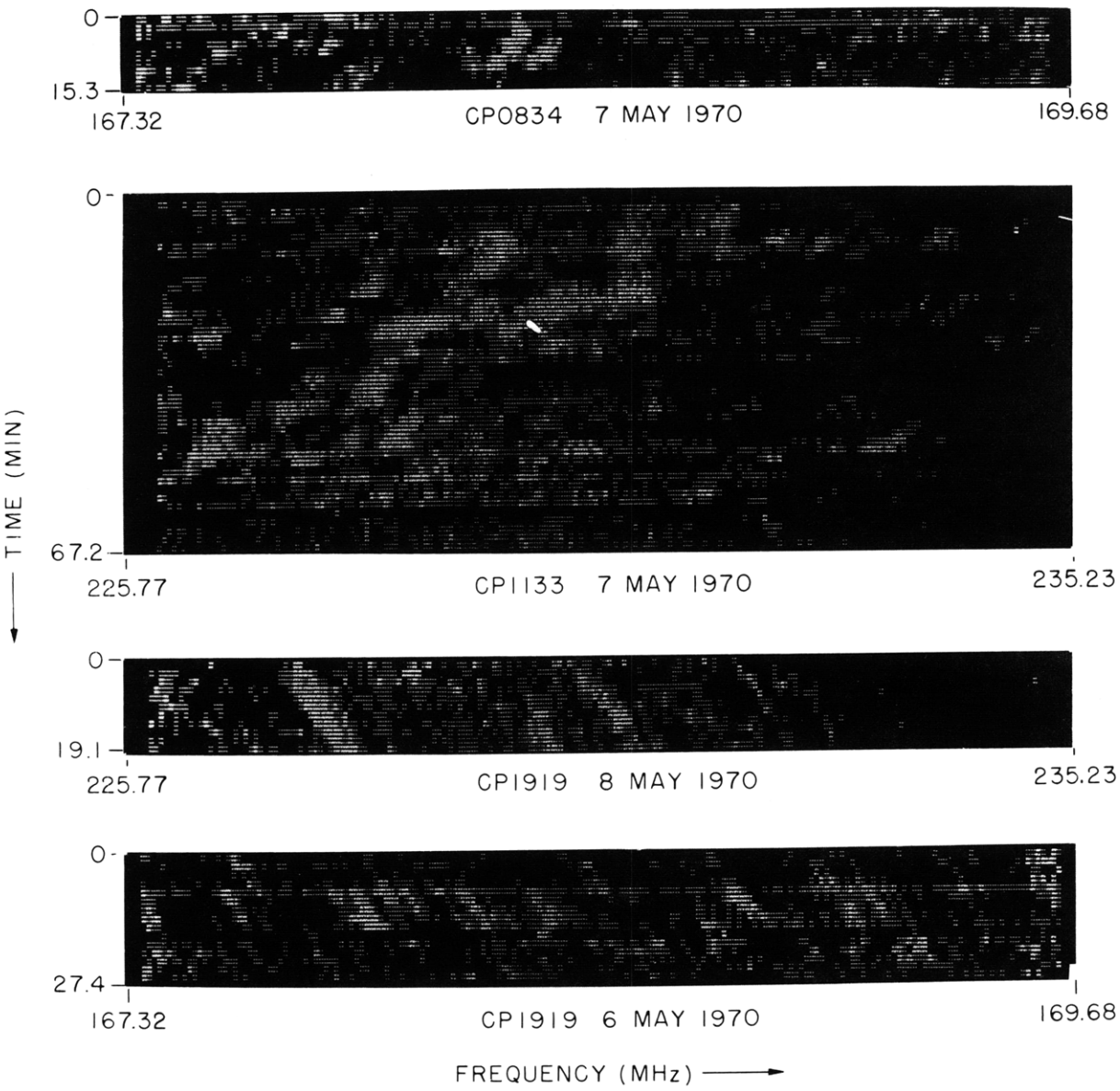

Fig. III-13. Dynamic spectra of CP0834, CP1133, and CP1919 taken with 384-channel autocorrelation receiver. Relative intensity ratios of 2:1 are represented by the two brightness levels.

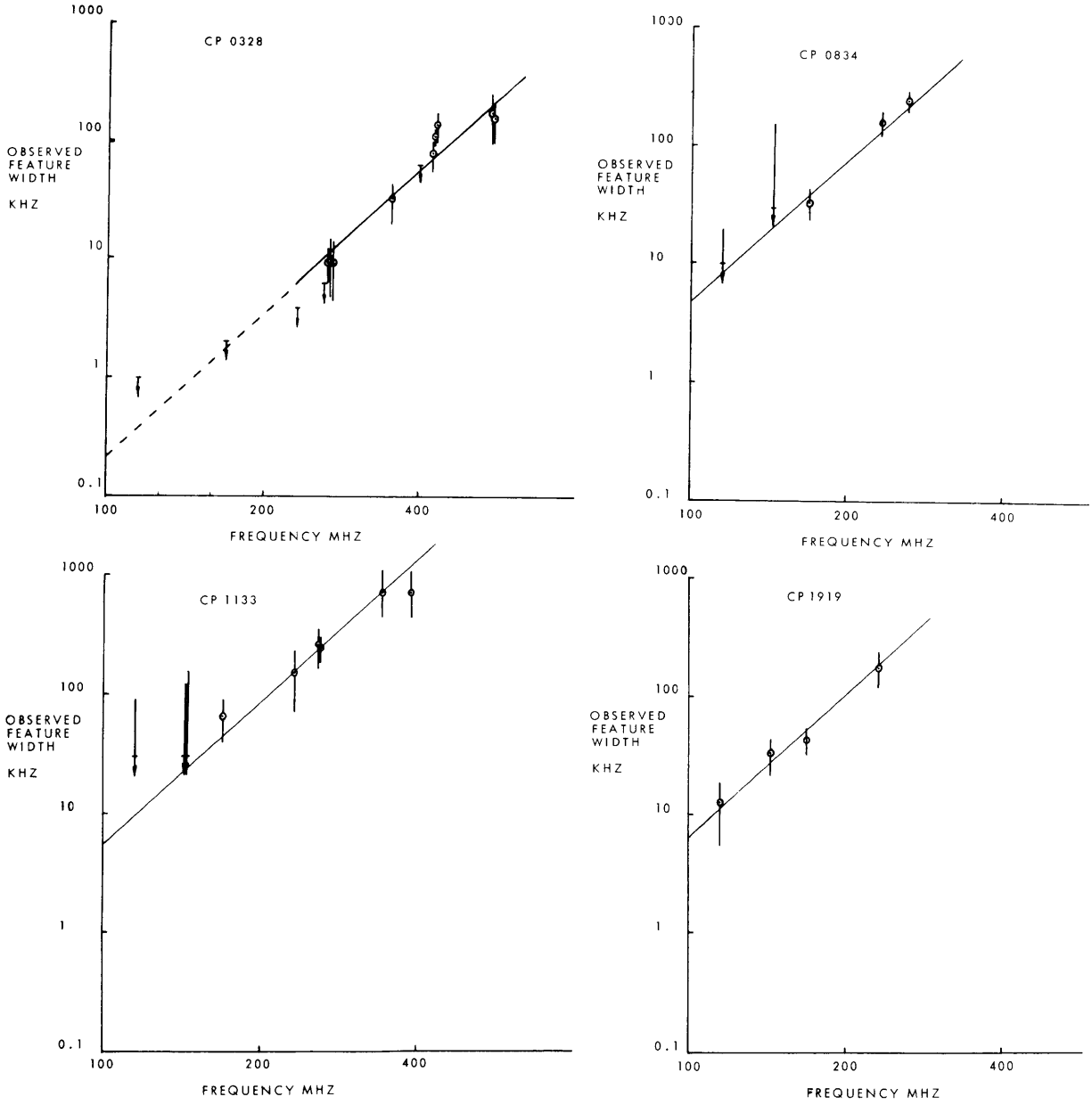

Fig. III-14. Wavelength dependence of spectral feature widths. Widths represent averages of many spectral features, and error bars indicate the total range of observed feature widths. Arrows and crossbars represent the limitations of spectral resolution. The sloping lines correspond to a ν^4 dependence of feature width.

have traversed different paths, and that the path lengths differ by a nominal value δ, where δ arises geometrically, and is approximately $R\theta_s^2/2$, where R is the distance to the pulsar, and θ_s is the rms angle of arrival of the ray at the antenna. This same model predicts that the spectral feature widths will also be approximately inversely proportional to the square of the dispersion measure, a result that is compatible with the present observations. Such scintillation models have been discussed by Scheuer,[5] Salpeter,[6] and Uscinski.[7, 8]

Table III-3. Pulsar spectral feature widths.

Source	Frequency (MHz)	B (kHz)	α	Source	Frequency (MHz)	B (kHz)	α
CP0328	112	<1 ?		CP1133	112	<90	
	168	$\lesssim$2			142	<150	
	267	10 ± 5			168	65 ± 25	
	350	33 ± 13			230	150 ± 80	
	405	111 ± 50			350	417 ± 70	
	560	170 ± 70	3.9 ± 0.8		405	692 ± 250	2.6 ± 0.6
CP0834	112	<20		CP1919	112	13 ± 7	
	142	<150			142	34 ± 10	
	168	34 ± 9			168	38 ± 20	
	230	162 ± 35			230	178 ± 60	3.5 ± 1.1
	258	245 ± 40	4.6 ± 0.5				

3. Drifting of Spectral Features

A very interesting property of some pulsars is systematic drifting of spectral features, as illustrated for CP1919 and CP1133 in Figs. III-12 and III-13. Drifting has been observed in each of these two pulsars on several occasions, although the phenomenon can be readily overlooked if the spectrometer resolution is not appropriate, or if the operating frequency is such that the drift rate is too slow or obscured by variations in intrinsic pulsar intensity. Drifting has also probably been observed in CP0834. Representative observed drift rates for CP0834, CP1133, and CP1919 are 130 Hz/s at 168 MHz, 1 kHz/s at 230 MHz, and 500 Hz/s at 230 MHz, respectively. The drift rates appear to vary from month to month, and may vary on shorter time scales. The drifts of both CP1919 and CP1133 have changed directions, and at times different simultaneous spectral features may have different drift rates.

A simple model for interstellar scintillation yields an understanding of spectral

drifting. We may assume that the radiation propagating from the pulsar to Earth is composed of rays, each executing a random walk characterized by θ_s, the rms angle between any ray segment and the direct path. These rays converge at the Earth with different arrival angles and different delays. If many scattering events occur for each ray, then the propagation delay and the angle of arrival may be weakly correlated, in contrast to the single thin-screen model.

Consider the case in which the radiation incident upon the Earth is dominated by two rays. The interference of the rays produces an interference pattern through which the Earth moves at velocity v_o. In this case the lifetime Δt of a single spectral feature, that is, the time between half-power points at a single frequency, is the time required for the Earth to move past one lobe of the interference pattern. That is,

$$\Delta t \cong \frac{\lambda}{\sqrt{8}\,\theta_s v_o},$$

where λ is wavelength, and $\sqrt{8}$ is an approximate geometrical factor. A frequency drift can result if the propagation delays for these two rays are different. The phenomenon is analogous to the movement of an observer through the frequency-dependent lobes of a transmitting interferometer. If the delays differ by the reasonable value $R\theta_s^2/2$, where R is the pulsar-Earth separation, then the feature drift rate $\dot{\nu}$ is

$$\dot{\nu} \cong \nu v_o \sqrt{\frac{8B}{Rc}}.$$

Since the nominal width B is proportional to $\nu^4 R^{-2}$, it follows that the drift rate $\dot{\nu}$ should be proportional to $\nu^3 R^{-3/2}$. Consistency of these expressions requires $\dot{\nu} \sim B/\Delta t$, where $B \cong c/R\theta_s^2$.

By averaging the drift rates of several spectral features, it is possible to estimate the magnitude and frequency dependence of the drift rates. Since rays of different frequencies have different interstellar propagation paths, and the paths are time-variant, many observations will be required. For the present limited data the drift rate is proportional to $\nu^{3\pm1.5}$. Although the observations are consistent with the $R^{-3/2}$ dependence upon pulsar distance, the results are not definitive. The drift rate predicted for CP0328 is approximately 70 Hz/s at 200 MHz, which is too small to be evident in the spectra of Fig. III-12.

The observations of $\dot{\nu}$ can yield an independent estimate of the transverse pulsar velocity v. We deduce approximate velocities of 100 km/s for all three pulsars using the drift rate, bandwidths, and equations cited here, and assuming that the interstellar electron density is 0.03 cm^{-3} (Staelin and Reifenstein[9]). This equals the velocities deduced from the feature lifetimes Δt. For example, for the data of Fig. III-12 and

Table III-3, the approximate velocity formula

$$v \cong \sqrt{\frac{cRB}{8}}\,\frac{1}{\nu\Delta t}$$

yields for CP0328, CP0834, CP1133, and CP1919 velocities of 100 km/s, within a factor of two. Rickett[1] and Lang[3] have deduced similar velocities from their feature-lifetime data. Further corroboration follows from the measurements by Lang and Rickett[10] of scintillation delay between spectral features observed at Arecibo and Jodrell Bank, which yielded velocities for CP1133 of approximately 100 km/s.

Since the velocity of the Earth with respect to the interstellar medium within 2 kpc is generally less than 50 km/s, these data suggest that the average transverse velocity of these three pulsars with respect to the interstellar medium may be of the order of 100 km/s, which is consistent with the velocities of runaway stars (Gott et al.,[11] Gunn and Ostriker,[12] and Prentice[13]) and of NP0531. More extensive drift rate data and more accurate theoretical analysis could further strengthen this conclusion.

The consistency of these spectral observations with theoretical models of interstellar scintillation further supports suggestions of Rickett[14] and others[15, 16] that the observed slow spectral changes originate in the interstellar medium. Our observations have extended this conclusion to spectral features of widths ranging from 2 kHz to several MHz.

We wish to thank J. M. Sutton for helpful conversations and acknowledge the cooperation and assistance of W. Brundage, J. Greenhalgh, and other staff members of the National Radio Astronomy Observatory.

M. S. Ewing, R. A. Batchelor, R. D. Friefeld,
R. M. Price, D. H. Staelin

References

1. B. J. Rickett, Nature 221, 158 (1969).
2. D. H. Staelin, contribution to Accademia Nazionale Dei Lincei Meeting on "Pulsars and High Energy Activity in Supernovae Remnants," 1969.
3. K. R. Lang, "Interstellar Scintillation of Pulsar Radiation" (Preprint, 1970).
4. G. R. Huguenin, J. H. Taylor, and M. Jura, Astrophys. Letters 4, 71 (1969).
5. P. A. G. Scheuer, Nature 218, 920 (1968).
6. E. E. Salpeter, Nature 221, 31 (1969).
7. B. J. Uscinski, Phil. Trans. Roy. Soc. London A262, 609 (1968).
8. B. J. Uscinski, Proc. Roy. Soc. London A307, 471 (1968).
9. D. H. Staelin and E. C. Reifenstein III, Science 162, 1481 (1968).
10. K. R. Lang and B. J. Rickett, Nature 225, 528 (1970).
11. J. R. Gott III, J. E. Gunn, and J. P. Ostriker, Astrophys. J. 160, L91 (1970).

12. J. E. Gunn and J. P. Ostriker, Astrophys. J. 160, 979 (1970).

13. A. J. R. Prentice, Nature 225, 438 (1970).

14. B. J. Rickett, Mon. Not. Roy. Astron. Soc. (in press).

15. J. M. Rankin, J. M. Comella, H. D. Craft, Jr., D. W. Richards, D. B. Campbell, and C. C. Counselman III (to appear in Astrophys. J.).

16. D. H. Staelin and J. M. Sutton, Nature 226, 69 (1970).